Proceedings of the
10th Graz Brain-Computer Interface Conference 2026

10.3217/978-3-99161-093-9-003

Unsupervised Intent Gating: Improving Calibration and Online Reliability in Motor Imagery BCIs

Paolo Forin[1], Stefano Tortora[1,2], Emanuele Menegatti[1,2] and Luca Tonin[1,2]

[1]Department of Information Engineering, University of Padova, Padova, Italy
[2]Padova Neuroscience Center, University of Padova, Padova, Italy

E-mail: paolo.forin@phd.unipd.it

ABSTRACT: Motor Imagery (MI) Brain-Computer Interfaces (BCIs) are frequently hampered by fluctuations in user attention, which introduce noisy labels during standard calibration. To address this, we propose an unsupervised gating architecture using a Gaussian Mixture Model (GMM) to dynamically estimate Intentional Control (IC). By evaluating sensorimotor rhythm spatial focality, the GMM automatically filters out non-informative idling segments without manual pruning. Offline validation (N=5) demonstrated sharper neurophysiological topographies and higher class separability than standard methods. During real-time closed-loop control, the GMM probability dynamically weighted a continuous soft-increment integrator. While baseline sample-wise accuracy remained comparable (77.7% vs. 77.4%), the gating mechanism effectively converted neural uncertainty into safe timeouts, boosting effective active decision accuracy to 92.7% and maintaining a 76.0% safety margin against false positives during rest. This intent-gated paradigm offers a robust framework for safe, real-world assistive BCI technologies.

INTRODUCTION

While Motor Imagery (MI) remains a cornerstone of non-invasive Brain-Computer Interfacing (BCI), the transition from controlled calibration to reliable online control is frequently hampered by the inherent non-stationarity of Electroencephalographic (EEG) signals [1, 2]. This reliability gap is particularly critical in neurorobotics, where safety and precision are paramount for controlling wheelchairs or telepresence robots [3]. A predominant factor degrading classifier generalisation is high intra-subject variability, often driven by fluctuations in the user's psychophysiological state [4–6]. Standard calibration protocols typically employ a synchronous approach where the system assumes a stable state of "Intentional Control" (IC) throughout the entire duration of the performed task. Consequently, supervised learning pipelines assign a static class label to all time points within this interval [7, 8]. However, neurophysiological and behavioural studies suggest that sustained attention during mental imagery is rarely constant. Factors such as cognitive fatigue, "mind-wandering," or delayed task initiation can introduce significant periods of "Intentional Non-Control" (INC) or idling states within the theoretically active trial [3, 9, 10]. From a machine learning perspective, this creates a "noisy labelling" problem: the classifier is forced to learn decision boundaries from a dataset where a subset of samples represents background noise. This ambiguity dilutes the separability of the feature space, ultimately reducing decoding accuracy [1, 11, 12]. To mitigate signal contamination, standard pipelines rely on artifact removal algorithms (e.g., Regression, ICA) to suppress EOG and EMG activity [13, 14]. While effective for physiological noise, these methods do not address "cognitive artifacts"—moments where the signal is clean, but the user's intent is absent [15]. Advanced geometric approaches, such as Riemannian Manifolds, have shown robustness to covariance shifts [16, 17], yet they typically remain supervised and susceptible to label noise. Another established strategy is shared control, where the intelligent system compensates for the BCI's uncertainty by handling low-level tasks (e.g., obstacle avoidance) [18]. In this scenario, there is a growing need for unsupervised or semi-supervised methods designed to explore the latent structure of the training data to isolate informative segments automatically [2, 19, 20]. In this study, we propose an unsupervised framework that integrates neurophysiological insights with machine learning to refine both BCI calibration and real-time continuous control. We hypothesise that effective motor imagery is characterised by high spatial focality compared to the resting state, so we apply a Gaussian Mixture Model (GMM) to a spatial focality feature. During the calibration phase, this probability-based gate automatically filters out non-informative idling segments from the training stream without requiring manual labels. By restricting the training of a Quadratic Discriminant Analysis (QDA) classifier to these GMM-verified samples, we achieve a sharper decision boundary, significantly boosting class separability (Fisher Score) and Signed R^2 while ensuring neurophysiological plausibility. Crucially, we extend this mechanism into the online closed-loop architecture, where the continuous GMM probability dynamically weights a soft-increment integrator. By doing so, the intent-gate actively translates user uncertainty into safe timeouts, drastically improving the effective decisional accuracy and providing a robust safety margin against false positives during resting states.

 10.3217/978-3-99161-093-9-003

MATERIALS AND METHODS

Data acquisition and experimental paradigm:
EEG data were recorded from 5 healthy subjects (age 26.5 ± 1.5) using a g.USBamp system. Signals were acquired at a sampling rate of 512 Hz from 16 active electrodes positioned according to the international 10-20 system, concentrated over the sensorimotor area (including Fz, FC3, FC1, FCz, FC2, FC4, C3, C1, Cz, C2, C4, Fp1, CP1, CPz, CP2, Fp2). Ground was placed at AFz and reference at the right earlobe. The experimental protocol was organised into a single recording session consisting of two distinct phases: calibration and online evaluation. The calibration phase was composed of three runs, designed to gather the necessary data for classifier training. Each subject performed 30 trials per Motor Imagery (MI) class (both feet and both hands), for a total of 60 calibration trials, where participants received always-correct visual feedback. Subsequently, the system's performance was assessed during the online evaluation phase, which included two runs. Each evaluation run consisted of 10 trials per MI class and 5 additional rest trials, totalling 25 trials per run, where real-time feedback reflected the user's control. Trials followed a standard cue-based synchronous paradigm (Fig. 1).

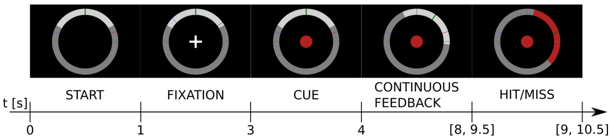

Figure 1: Trial organization: first the fixation (duration 2s), then a visual cue (duration 1s), which can be red/blue/yellow (both hands/both feet/rest), then the continuous feedback (the duration in the calibration is a random number between 4 to 5.5s, while in evaluation the max duration is 10s) and lastly the hit/miss (duration 1s).

Signal preprocessing:
Signal processing was performed using MATLAB (MathWorks, Natick, MA). First, a Common Average Reference (CAR) spatial filter was applied to enhance the signal-to-noise ratio. The signal was then filtered into two frequency bands of interest: μ (8–13 Hz) and β (18–24 Hz) using a 4th-order Butterworth filter. To extract the temporal envelope of the signal, we applied the Hilbert Transform, computing the instantaneous power. A moving average filter with a 1-second buffer was applied to smooth the power features. Before further analysis, an artefact rejection stage was implemented to remove high-amplitude noise. Trials contaminated by eye movements (EOG) or excessive muscle activity (EMG) were identified using threshold-based criteria on specific channels (Fp1, Fp2 for EOG) and rejected from the dataset.

Spatial focality feature extraction:
To distinguish between IC and INC states within a trial, we introduced a high-level feature quantifying the "spatial focality" or focality of the motor activation. For each time sample t, we computed the mean power in three Regions of Interest (ROIs): Left (ROI_L: C3, C1, CP1), Right (ROI_R: C4, C2, CP2), and Centre (ROI_C: Cz, FCz, CPz). The focality feature F(t) is defined as the log-ratio between the median power and the minimum power of the ROIs:

$$F(t) = log(\frac{median(P_{ROI})}{min(P_{ROI})}) \tag{1}$$

where $P_{ROI} = [P_{ROI_L}, P_{ROI_R}, P_{ROI_C}]$. This metric increases when a specific motor area exhibits strong desynchronization (ERD), indicating a focused high-control state. The choice of this specific feature is driven by the neurophysiological nature of Motor Imagery (MI). While the resting state is typically characterised by widespread synchronised activity (high power) across the sensorimotor cortex, MI induces a focal Event-Related Desynchronization (ERD) in the contralateral hemisphere. By computing the log-ratio between the median power (representing the background activity) and the minimum power (representing the active region), we obtain a metric with 2 characteristics: 1) Class-Agnostic: The min operator automatically identifies the active hemisphere without requiring prior knowledge of the task. 2) Robust to Non-Stationarity: The ratio normalises local activation against the current global power level, making the feature resilient to global drifts in EEG amplitude caused by fatigue or impedance changes. As a result, F(t) yields low values close to zero during synchronised resting states (where $median \approx min$) and high positive values during focal motor control (where $median > min$).

Unsupervised GMM gating:
We classified the distribution of the spatial focality feature, $F(t)$, using a Gaussian Mixture Model (GMM) with $K = 2$ components, corresponding to two latent states: High Focus (IC) and Low Focus/Rest (INC). Before GMM fitting, the calibration features were normalised. The model was configured with full, unshared covariance matrices and a regularisation parameter of 10^{-5}. The cluster exhibiting the higher mean focality was automatically designated as the IC state. We then computed the posterior probability $P(IC \mid F(t))$ for each sample and applied a threshold-based gating policy. This allowed us to construct an optimised training set for the subsequent MI-QDA classifier:

$$gate(F(t)) = \begin{cases} 1 & if \;\; P(IC \mid F(t)) \geq 0.5 \\ 0 & otherwise \end{cases} \tag{2}$$

To construct an optimised training set, we applied a threshold-based policy where only samples satisfying $gate(F(t)) = 1$ were retained. The threshold 0.5 ensures that the MI-QDA classifier is trained on data with a higher probability of belonging to the IC cluster. This mechanism effectively prunes intra-trial idling periods. To validate the overall proposed method, we compared two strategies: 1) Standard Calibration: Using all time samples within the cue period. 2) GMM-Gated Calibration: Using only the samples selected by the GMM.
In addition, we divide the calibration data into train-test

 10.3217/978-3-99161-093-9-003

(75%-25%) and for both strategies, we assessed the improvement in data quality, looking at: 1) Fisher Score: To quantify the discriminative power of the features for each channel and frequency band. 2) Signed R-squared: To measure the correlation between the spectral power and the class labels, providing a neurophysiological validation of the selected signal patterns. For the online evaluation, the GMM parameters were estimated using the entire calibration dataset and kept fixed during closed-loop control.

***Online gated control architecture**:*
The calibration framework was translated into a real-time closed-loop system implemented within the ROS-Neuro middleware [21]. The online pipeline processes incoming EEG data streams in chunks of 32 samples (hence there is a downsample from 512 Hz to 16 Hz) and is composed of three hierarchical stages as follows:

1. Shared Signal Processing Pipeline
To ensure consistency between calibration and online control, the real-time system employs the exact same preprocessing chain used in the offline analysis. The raw signal is spatially filtered via CAR, band-pass filtered in the μ (8–13 Hz) and β (18–24 Hz) bands, and the instantaneous power envelope is extracted via Hilbert transform using a ring buffer of 1 second.

2. Parallel Probabilistic Estimation
At each time step t, the system computes two independent probabilistic metrics in parallel:

- Intent Detection (The Gate): The spatial focality feature $F(t)$ is extracted from the motor ROIs. The pre-trained GMM computes the posterior probability of IC $P(IC \mid F(t))$.
- Task Classification (The Direction): Simultaneously, the pre-trained QDA classifier computes the class posterior probabilities $P(QDA_t \mid x_t)$ (e.g., hands vs. feet) based on the band power features.

3. Reliability-Weighted "Soft" Integration
The core of the control logic is a dynamic accumulation framework defined as a "Soft-Increment" Integrator. Instead of using a raw classifier output, the system first computes a merged control probability $P_{merged}(t)$ by modulating the QDA output with the GMM confidence:

$$P_{merged} = P(IC) \cdot P(QDA) + (1 - P(IC)) \cdot 0.5 \quad (3)$$

This formulation ensures that as the user focus drops ($P(IC \mid F(t)) \approx 0$), the signal converges to the neutral state (0.5). Crucially, the control signal update rate is not constant. The integration velocity $v(t)$ is computed as the normalised deviation from neutrality:

$$v(t) = min(1, \mid (P_{merged}(t) - 0.5) \mid \cdot 2 \cdot K_{gain}) \quad (4)$$

K_{gain} is a subject-specific gain empirically tuned to balance system responsiveness and stability. The final control command $C(t)$ is updated at each step:

$$C(t+1) = C(t) + sign(P_{merged}(t) - 0.5) \cdot \frac{\mid v(t) \mid}{b_s} \quad (5)$$

	c7	d7	i1	i2	m1
μ	0.87	0.92	0.82	0.84	0.93
β	0.89	0.78	0.85	0.96	0.86

Table 1: Pearson correlation coefficients (R) between Spatial Sparsity and GMM Confidence.

where, b_s is a fixed parameter set to 64, which defines the system's control horizon. Given the system's update rate of 16 Hz, this b_s establishes a nominal saturation time of 2 seconds. However, expecting the user to reach full saturation (C(t)=1.0) often leads to fatigue, as it requires maintaining perfect classification accuracy for the entire window. To improve responsiveness, we implemented an activation threshold (e.g., $Th_{act} = 0.8$). The system triggers the command as soon as $C(t) \geq Th_{act}$. This allows the user to execute tasks efficiently once sufficient cumulative evidence is gathered, without the need to drive the integrator to its asymptotic limit.
This architecture provides a dual advantage: the Gating mechanism ($P(IC \mid F(t))$) strictly pauses integration during resting states (reducing False Positives), while the Soft-Increment logic (K_{gain}) allows decoupling the system's responsiveness from the buffer length, enabling faster reactions for experienced users when confidence is high.

RESULTS

***GMM behaviour and feature validation**:*
We first analysed the relationship between the extracted spatial focality features and the posterior probabilities $P(IC \mid F(t))$ generated by the GMM on the test set. This validation was performed separately for the μ (8–13 Hz) and β (18–24 Hz) frequency bands across all five subjects. Fig. 2a illustrates the trend of the focality feature as a function of the GMM confidence. In both frequency bands, a strictly monotonic positive relationship is observed across all subjects (reported in the Tab. 1). More in detail in the μ band (8–13 Hz), the Pearson correlation coefficients (R) indicate a strong linear dependency, ranging from a minimum of R=0.82 (Subject i1) to a maximum of R=0.93 (Subject m1). While in the β band (18–24 Hz), the correlations remain high, ranging from R=0.78 (Subject d7) to R=0.96 (Subject i2). Error bars indicate the standard error of the mean for each confidence bin. Fig 2b displays the probability density of the GMM confidence scores ($P(IC)$) grouped by subject. The distributions exhibit a bimodal behaviour with data accumulating at the extremes ($P(IC) \leq 0.1$ and $P(IC) \geq 0.9$). Notable inter-subject variability is observed in the proportion of high-confidence samples. For example, in Fig. 2b Subject i1 (yellow bars) shows a dominant peak in the low-confidence region, indicating a prevalence of resting or non-focal states during the calibration trials. Conversely, Subjects c7 (blue bars) and m1 (green bars) display a higher density of samples in the high-confidence region, suggesting a more stable generation of focal motor patterns.

***Enhancement of calibration data quality**:*

10.3217/978-3-99161-093-9-003

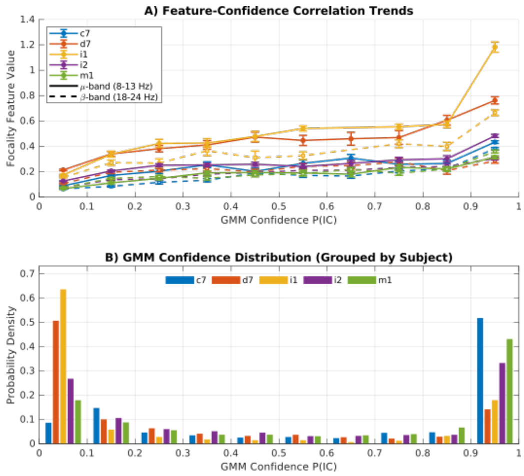

Figure 2: Validation of the unsupervised GMM gating model on the test set. (A) Correlation analysis between the extracted Spatial Sparsity feature and the GMM posterior probability of IC ($P(IC)$). Solid lines represent the μ band (8–13 Hz), while dashed lines represent the β band (18–24 Hz). Error bars denote the Standard Error of the Mean (SEM). (B) Grouped probability density of GMM confidence scores.

To quantify the benefit of the proposed unsupervised gating mechanism, we evaluated the discriminative power of the features extracted from the GMM-selected segments ($P(IC) \geq 0.5$) compared to the Standard calibration approach (using all data within the trial window). Furthermore, we analysed the rejected segments ($P(IC) < 0.5$) to assess the discarded data. All analyses report the grand average across the five subjects on the test set (25% of the calibration trials).

Quantitative analysis (Fisher score and R-square)

Fig. 3 presents the class separability and correlation metrics, analysed separately for the μ (8–13 Hz, left column) and β (18–24 Hz, right column) frequency bands. In both frequency bands, the GMM-selected data (red bars) yielded consistently higher mean separability compared to the standard approach (grey bars) over key sensorimotor channels. Channel by channel non-parametric statistics (Friedman and Wilcoxon) confirmed this enhancement: in the β band, the gating mechanism significantly increased the discriminative power over the primary sensorimotor channel C1 ($p < 0.05$, denoted by *). Furthermore, the GMM dataset demonstrated a marked increase in absolute R^2 coefficients, reflecting an improved Signal-to-Noise Ratio (SNR) while preserving the physiological directionality of task-related modulations (e.g., the negative correlation peak at Cz). Conversely, the rejected data (blue bars) exhibited lower discriminative power and higher cross-subject variability. Statistical comparisons proved that the GMM-isolated intent patterns were significantly superior to these rejected segments over specific channels (CP1 in μ band, FC4 in β band; p<0.05, denoted by *), confirming that the mechanism safely discards non-informative idling periods.

Neurophysiological validation

The topographic distribution of cortical activity visually corroborates the quantitative metrics. Fig. 4 illustrates the grand average difference maps (Class 1 minus Class 2) for the μ (left) and β (right) frequency bands. The GMM-selected data (top row) retain defined and highly contrasted activation patterns over the sensorimotor areas. In comparison, the standard full-window approach (middle row) yields spatially similar but noticeably attenuated topographies, demonstrating how the inclusion of idling or low-confidence segments dilutes the overall signal intensity. Interestingly, the rejected data (bottom row) still exhibit high-amplitude spectral differences; however, their spatial configuration is noticeably altered.

Online control performance:

The final validation of the proposed architecture was conducted through a real-time, closed-loop control session. To assess the impact of the unsupervised gating mechanism, we evaluated the performance at both the single-sample (frame-by-frame) and system (continuous trial) levels. The quantitative results across the five subjects are summarised in Tab. 2. Although real-time control was driven by QDA_{OUR}, comparison with offline-reconstructed QDA_{TRAD} performance showed comparable sample-wise decoding power ($77.4 \pm 12.7\%$ vs. $77.7 \pm 12.7\%$), indicating that GMM-based filtering preserves robust spatial patterns without degrading baseline model performance. This indicates that filtering the calibration dataset preserves the robust spatial patterns necessary for baseline classification without degrading the underlying model performance. The true advantage of the proposed architecture emerges at the system level, where the sample-wise probabilities are processed by the reliability-weighted integrator. The system achieved a grand average active trial accuracy of $77.5 \pm 12.6\%$ (Acc_{ACT}). Crucially, when excluding the runs that reach the timeouts to evaluate only the trials where the system reached a final decision ($Acc_{ACT_{noT}}$), the accuracy rise to $92.7 \pm 7.1\%$. This demonstrates that the GMM gate effectively translates user uncertainty or loss of focus into safe timeouts rather than executing erroneous commands. This high decisional reliability was achieved with a grand average timeout rate of only $16.5 \pm 5.4\%$, calculated as the ratio between the number of trials without a decision and the total number of trials. Finally, the system's safety margin was evaluated during the Idle task. The rest trial accuracy (Acc_{REST}), defined as the ability to suppress false positives while the user is not actively intending to control the BCI, reached a grand average of $76.0 \pm 19.5\%$.

DISCUSSION AND CONCLUSION

The development of reliable BCIs for real-world applications requires systems capable of autonomously distinguishing IC from spontaneous neural fluctuations. This study introduced an unsupervised gating architecture driven by a Gaussian Mixture Model (GMM), and the results demonstrate that this approach is highly effective and fundamentally grounded in neurophysiology.

The choice of using spatial focality as the primary

 10.3217/978-3-99161-093-9-003

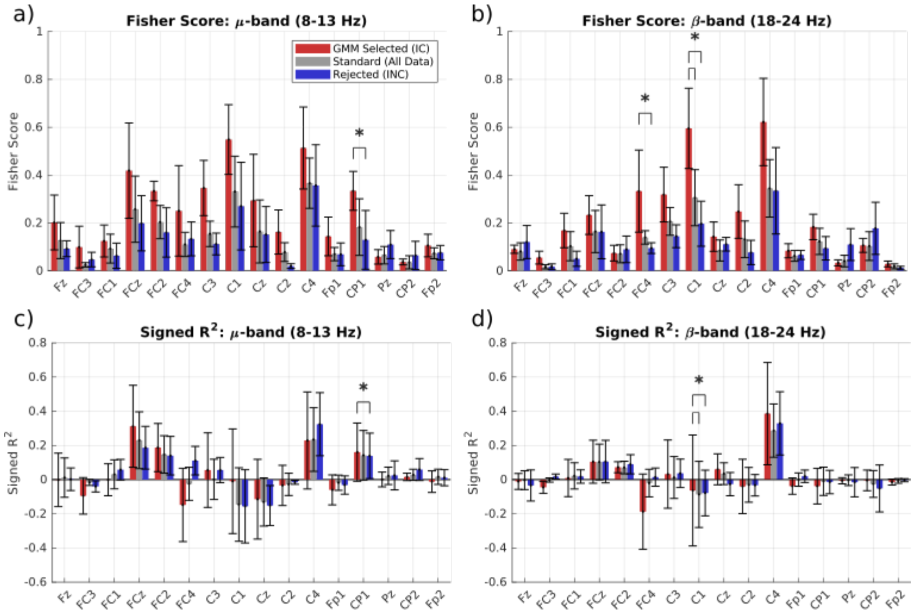

Figure 3: Quantitative assessment of calibration data quality across frequency bands. To account for inter-subject baseline variability, all metrics were subject-wise max-normalised prior to averaging. Top Row: Normalised Discriminative Power (Fisher Score) for the μ (left) and β (right) bands. The GMM-selected dataset (Red) demonstrates superior class separability compared to the full-window Standard method (Grey). Bottom Row: Normalised Class Correlation Direction (Signed R^2). The unsupervised gating amplifies the correlation magnitude (SNR) while preserving the physiological directionality of the signals. The Rejected data (Blue) consistently exhibits the lowest task-relevant modulation. Error bars represent the Standard Error of the Mean (SEM). Statistical significance between the GMM-selected dataset and either the Standard or Rejected approaches over key channels is denoted by asterisks (* p<0.05, one-sided Wilcoxon signed-rank test).

	c7	d7	i1	i2	m1	mean
QDA_{OUR}	61.2±4.0	93.5±1.4	80.5±9.5	83.3±2.7	68.7±0.2	77.4±12.7
QDA_{TRAD}	63.6±1.2	94.2±1.0	76.2±7.7	86.3±3.3	68.1±5.7	77.7±12.7
Acc_{ACT}	62.5±3.5	72.5±3.5	85.0±7.1	95.0±0.0	72.5±10.6	77.5±12.6
$Acc_{ACT_{noT}}$	86.2±0.7	100.0±0.0	91.8±4.1	100.0±0.0	85.4±1.7	92.7±7.1
Acc_{REST}	90±14.1	100.0±0.0	70±14.1	70.0±14.1	50.0±14.1	76.0±19.5
$Timeout_{RATE}$	27.5±3.5	27.5±3.5	7.5±3.5	5.0±0.0	15.0±14.1	16.5±5.4

Table 2: Online accuracy. Each raw report the mean and the standard deviation of the two online runs.

feature to train the GMM proved to be highly logical and physiologically sound. Genuine Motor Imagery elicits localised Event-Related Desynchronization/Synchronisation (ERD/ERS) over the sensorimotor cortex. By evaluating spatial focality, the GMM captures this focalization, easily discriminating between the localised activity of Intentional Control (IC) and the diffuse, non-informative patterns characteristic of idling states (INC). This physiological rationale is strongly validated by the offline analysis (Fig. 2 and Fig. 3), where the GMM successfully isolated the most informative SMR segments, yielding sharper spatial topographies and higher class separability without requiring any manual data pruning (Fig. 4). During the online closed-loop session, the integration of the GMM probability as a dynamic weight for the control command demonstrated crucial benefits for both active and rest tasks. For active trials, the gating mechanism ensures that the system accumulates evidence only when the user is focused. By converting uncertain neural fluctuations into safe timeouts rather than erroneous executions, the effective decision accuracy (excluding timeouts) reached 92.7%. Equally important is the system's behaviour during the rest task. The GMM probability fundamentally alters the integrator's dynamics: whenever the spatial focality drops (indicating a loss of focus or an intentional idle state), the GMM acts as a stabilising weight that actively pulls the control command back to a central, neutral resting state between the two classes. This mechanism successfully throttled the accumulator during non-intentional periods, maintaining an average safety margin of 76.0% against false positives.

Despite these systemic improvements, some limitations of the current study must be acknowledged. First, the online sample-wise accuracy of the Informed QDA did not show a massive improvement over the Standard QDA ($77.7\% vs. 77.4\%$). This indicates that while the GMM cleans the calibration data effectively, the primary benefit of the proposed architecture lies in the temporal gating of the integrator rather than a raw boost in frame-by-frame

10.3217/978-3-99161-093-9-003

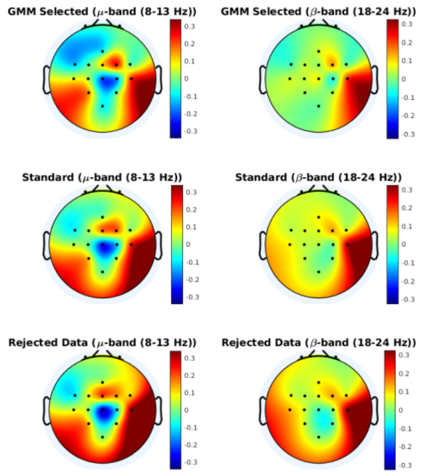

Figure 4: Neurophysiological Validation of the spatial activation patterns. Topographic maps illustrate the mean difference in spectral power between the two motor imagery classes for the μ band (8–13 Hz, left column) and the β band (18–24 Hz, right column). Top Row: The GMM-selected dataset. Middle Row: The Standard full-window. Bottom Row: The rejected dataset.

classification power. Second, the current implementation is restricted to a two-class paradigm. Finally, the validation was conducted on a limited cohort of five subjects with a small number of runs.

In conclusion, this paper presents a robust, unsupervised framework that significantly enhances the safety and reliability of Motor Imagery BCIs. By leveraging a physiologically meaningful GMM to dynamically weight the continuous control command, the system effectively manages both active control and resting states, minimising dangerous false positive activations. While further validation on larger cohorts and multi-class extensions is necessary, this intent-gated architecture provides a highly practical and scalable solution for bridging the gap between laboratory research and safe, real-world assistive technologies.

REFERENCES

[1] Shenoy P, Krauledat M, Blankertz B, Rao RPN, Müller KR. Towards adaptive classification for BCI. J. Neural Eng.. 2006;3(1):R13–23.

[2] Vidaurre C, Sannelli C, Müller KR, Blankertz B. Co-adaptive calibration to improve BCI efficiency. J. Neural Eng.. 2011;8(2):025009.

[3] Tonin L, Millán JdR. Noninvasive brain–machine interfaces for robotic devices. Annu. Rev. Control Robot. Auton. Syst.. 2021;4(1):191–214.

[4] Saha S, Baumert M. Intra- and inter-subject variability in EEG-based sensorimotor brain computer interface: A review. Front. Comput. Neurosci.. 2019;13:87.

[5] Jeunet C, N'Kaoua B, Subramanian S, Hachet M, Lotte F. Predicting mental imagery-based BCI performance from personality, cognitive profile and neurophysiological patterns. PLoS One. 2015;10(12):e0143962.

[6] Arvaneh M, Guan C, Ang KK, Quek C. Optimizing spatial filters by minimizing within-class dissimilarities in electroencephalogram-based brain-computer interface. IEEE Trans. Neural Netw. Learn. Syst.. 2013;24(4):610–619.

[7] Pfurtscheller G, Neuper C. Motor imagery and direct brain-computer communication. Proc. IEEE Inst. Electr. Electron. Eng.. 2001;89(7):1123–1134.

[8] Lotte F et al. A review of classification algorithms for EEG-based brain–computer interfaces: A 10 year update. J. Neural Eng.. 2018;15(3):031005.

[9] Millán JDR et al. Combining brain-computer interfaces and assistive technologies: State-of-the-art and challenges. Front. Neurosci.. 2010;4.

[10] Leeb R, Tonin L, Rohm M, Desideri L, Carlson T, Millan JdR. Towards independence: A BCI telepresence robot for people with severe motor disabilities. Proc. IEEE Inst. Electr. Electron. Eng.. 2015;103(6):969–982.

[11] Lemm S, Blankertz B, Dickhaus T, Müller KR. Introduction to machine learning for brain imaging. Neuroimage. 2011;56(2):387–399.

[12] Frénay B, Verleysen M. Classification in the presence of label noise: A survey. IEEE Trans. Neural Netw. Learn. Syst.. 2014;25(5):845–869.

[13] Schlögl A, Keinrath C, Zimmermann D, Scherer R, Leeb R, Pfurtscheller G. A fully automated correction method of EOG artifacts in EEG recordings. Clin. Neurophysiol.. 2007;118(1):98–104.

[14] Fatourechi M, Bashashati A, Ward RK, Birch GE. EMG and EOG artifacts in brain computer interface systems: A survey. Clin. Neurophysiol.. 2007;118(3):480–494.

[15] Lotte F, Larrue F, Mühl C. Flaws in current human training protocols for spontaneous Brain-Computer interfaces: Lessons learned from instructional design. Front. Hum. Neurosci.. 2013;7:568.

[16] Barachant A, Bonnet S, Congedo M, Jutten C. Multiclass brain-computer interface classification by riemannian geometry. IEEE Trans. Biomed. Eng.. 2012;59(4):920–928.

[17] Yger F, Berar M, Lotte F. Riemannian approaches in Brain-Computer interfaces: A review. IEEE Trans. Neural Syst. Rehabil. Eng.. 2017;25(10):1753–1762.

[18] Tonin L, Leeb R, Tavella M, Perdikis S, Millan JdR. The role of shared-control in BCI-based telepresence. 2010 IEEE International Conference on Systems, Man and Cybernetics - SMC. 2010.

[19] Kindermans PJ, Verstraeten D, Schrauwen B. A bayesian model for exploiting application constraints to enable unsupervised training of a p300-based BCI. PLoS One. 2012;7(4):e33758.

[20] Verhoeven T, Hübner D, Tangermann M, Müller KR, Dambre J, Kindermans PJ. Improving zero-training brain-computer interfaces by mixing model estimators. J. Neural Eng.. 2017;14(3):036021.

[21] Tonin L, Beraldo G, Tortora S, Menegatti E. ROS-neuro: An open-source platform for neurorobotics. Front. Neurorobot.. 2022;16:886050.